Automotive Science and Engineering, Vol. 16, No. 1, (2026), 4906-4921

Iran University of Science and Technology

Automotive Science and Engineering

Journal Homepage: ase.iust.ac.ir

ISSN: 2008-9899

Experimental and Numerical Investigation of the Effects of Linear and Nonlinear Modeling on the Performance of a Polymer Ball Dual Mass Flywheel in Reducing Engine Torque Fluctuations

Seyed Ali Mousavi[1*], Saeed Mahjoub Moghadas[2*], Hosein Mansouri[3]

[1]Ph.D. , Mechanical Engineering Department ,Imam Hossein University, Tehran, Iran

[2]Associate professor, Mechanical Engineering Department ,Imam Hossein University, Tehran, Iran

[3]Assistant professor, Mechanical Engineering Department ,Imam Hossein University, Tehran, Iran

ARTICLE INFO

Article history:

Received : 21 Mar 2025

Accepted: 18 Dec 2025

Published: 7 Jan 2026

Keywords:

Dual-mass flywheel

Power transmission system

torque fluctuations

linear modeling

nonlinear modeling

dynamometer testing

A B S T R A C T

In the automotive industry, reducing torsional vibrations caused by combustion irregularities and internal inertial forces is essential for improving powertrain quality, NVH (Noise, Vibration, and Harshness), and component durability. This study introduces and analyzes an innovative dual mass flywheel (DMF) with polymer bearings, aimed at enhancing torsional damping and ensuring smoother torque transmission in six-cylinder gasoline engines. The DMF consists of two masses, low-stiffness springs, and polymer bearings, all thoroughly modeled. Both linear and nonlinear dynamic analyses were performed, incorporating factors such as centrifugal force, nonlinear friction, and viscous damping. Component parameters were obtained via modal tests and experimental measurements. To validate the model, cylinder pressure and torque data were collected using sensors and a dynamometer, then compared with simulation results. Results reveal that employing the DMF reduces output torque fluctuations by up to 89.9% and significantly increases torsional vibration damping without a notable weight increase. Compared with a single-mass flywheel of equal inertia, the DMF decreased torque fluctuation amplitude by 46%, 41%, and 38% at 2250, 3000, and 3750 rpm, respectively. Achieving similar damping with a single-mass flywheel would require over an 80% mass increase. The nonlinear model provided a close match to experimental data, with simulation error below 5%. Overall, this integrated approach demonstrates that the dual mass flywheel with polymer bearings improves dynamic engine performance, NVH, and powertrain durability. These findings support the development of lighter, more advanced powertrain systems for next-generation vehicles.

1. Introduction

Torsional vibrations in automotive powertrains remain a major challenge in improving NVH (Noise, Vibration, and Harshness) performance, passenger comfort, and drivetrain durability. These vibrations primarily originate from cyclic combustion pressure variations and inertial forces associated with reciprocating engine components, leading to torque fluctuations transmitted to the transmission system. Conventional torsional dampers, such as clutch-based systems, suffer from limited torsional compliance and relatively high stiffness, which restrict their effectiveness over wide engine sspeed ranges. Consequently,

*Corresponding Author
Email Address: smahjoubmoghadas@ihu.ac.ir
http://doi.org/10.22068/ase.2026.721

[DOI: 10.22068/ase.2026.721]

more advanced vibration mitigation solutions have been developed.

Among these solutions, the dual-mass flywheel (DMF) has proven to be one of the most effective devices for torsional vibration attenuation. By employing low-stiffness arc springs and allowing large relative angular displacement between the primary and secondary masses, DMFs significantly reduce the natural frequency of the powertrain system and shift resonance below engine idle speed, thereby preventing resonance during normal operating conditions [1]. Owing to these advantages, extensive research has been conducted on DMF modeling, design, and experimental validation.

The dynamic behavior of DMFs has been investigated from different perspectives. In particular, research has addressed stiffness nonlinearity and hysteresis effects [2], secondary oscillations and control strategies [3], damping modeling based on relative angular velocity [4], and speed-dependent friction behavior of arc springs [5]. The influence of clearance, friction, and operating conditions on DMF-equipped rotor systems has also been numerically and experimentally examined [6–8]. In parallel, significant progress has been made in experimental DMF characterization, including high-precision angular displacement measurement systems [9,10], reduced-order dynamic modeling [11], start-up resonance and failure mechanisms [12], fatigue life enhancement [13], and semi-active DMFs employing magnetorheological fluids [14]. Shojaei et al. [15] validated torsional vibration models of a six-cylinder engine through numerical and experimental comparison, demonstrating the importance of accurate dynamic representation for durability assessment. Song et al. [16] introduced a DMF with continuously variable stiffness, effectively isolating resonance from the main operating range. Chen et al. [17] showed that nonlinear DMF models incorporating hysteresis and stick–slip behavior provide significantly better agreement with experimental data than linear models. Multi-stage and hybrid powertrain applications of DMFs were numerically investigated by Wang et al. [18] and Tang et al. [19], confirming notable improvements in NVH performance. Parametric investigations by He et al. [20] and nonlinear analyses by Maghsoudi et al. [21] further demonstrated the critical role of inertia ratio selection and nonlinear effects in torsional vibration attenuation. Additionally, studies on DMF durability and drivetrain loading [22] and comprehensive engine dynamic modeling frameworks [23] have contributed to a deeper understanding of torsional vibration mechanisms in modern powertrains.

In parallel, Berbyuk conducted a series of influential studies on optimized torsional vibration absorbers for heavy-duty powertrains. In an initial investigation, Berbyuk [24] examined the feasibility of applying a dual-mass flywheel to heavy-duty truck drivetrains, focusing on dominant engine-order excitations and employing global sensitivity analysis and Pareto-based multi-objective optimization to identify optimal inertia, stiffness, and damping parameters. Subsequently, Berbyuk [25] introduced a triple-mass flywheel (TMF) and formulated a weight–vibration Pareto optimization framework, demonstrating that an optimized TMF can outperform a conventional DMF in torque oscillation attenuation without a significant increase in total mass inertia. In a later study, Berbyuk [26] revisited the DMF concept and showed that weight–vibration optimized DMFs can simultaneously achieve effective torque fluctuation reduction and lightweight design requirements over a wide engine speed range. Despite these extensive studies, the combined effects of nonlinear dynamic modeling, speed- and load-dependent friction forces, and innovative damping mechanisms—such as polymer bearings or polymer-based elements—have not yet been investigated in an integrated and systematic manner, particularly with comprehensive experimental validation and direct comparison between numerical and dynamometer test results.

Accordingly, the present study addresses this research gap through an integrated numerical and experimental investigation of a novel dual-mass flywheel incorporating polymer bearings for a six-cylinder gasoline engine. Both linear and nonlinear dynamic models are developed, explicitly accounting for centrifugal effects, nonlinear friction, and viscous damping. The numerical predictions are validated using extensive dynamometer testing based on measured cylinder pressure and torque data. The results demonstrate the superior accuracy of nonlinear modeling and highlight the effectiveness of polymer-based torsional damping mechanisms in significantly reducing engine torque fluctuations while avoiding excessive mass increase.

2. Introduction of the dual-mass flywheel with polymer balls

In the novel dual mass flywheel (DMF) design incorporating polymer bearings (its general layout

[DOI: 10.22068/ase.2026.721]

is depicted in Figure 1) the assembly consists of four main components:

1. Primary Flywheel: This part is directly connected to the end of the engine crankshaft and serves as the mounting position for the starter ring gear.

2. Secondary Flywheel (Secondary Mass): This component is attached to the transmission input shaft via its central spline and functions to transmit rotational force to the drivetrain.

3. Independent Springs: A set of low-stiffness springs positioned between the primary and secondary flywheels; their function is to absorb and attenuate the engine's torque fluctuations.

4. Polymer Bearings: These bearings are also installed between the two flywheels and, similar to the springs, enable controlled relative rotational movement between the flywheels. The presence of polymer bearings ensures that the rotational motion of the two flywheel plates relative to each other occurs without direct contact and excessive wear.

The operational process of this assembly is as follows: When the engine starts, the crankshaft and consequently the primary flywheel begin to rotate. The force and torque produced by the crankshaft are first transmitted to the primary flywheel and then, through the springs which compress in response to increased torque are gradually transferred to the secondary flywheel. In this manner, engine torque is delivered to the transmission in an indirect and controlled fashion.

A key aspect of this design is the simultaneous use of soft springs and polymer bearings, which effectively reduces the amplitude of torque fluctuations and the impact loads transmitted from the engine to the powertrain. As a result, the input torque to the gearbox is significantly smoother and more uniform, leading to noticeably reduced system vibration and noise, and ultimately improving the overall performance of the power transmission system.

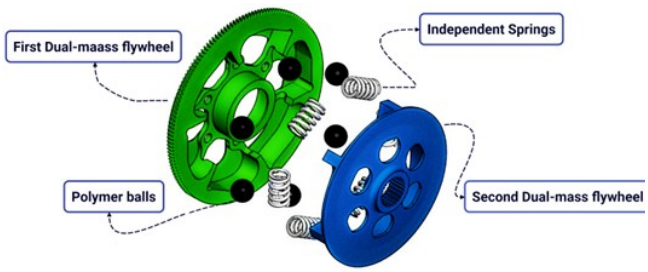

Figure 1: Schematic of a dual-mass flywheel with polymer balls.

3. Dynamic Analysis of a Six-Cylinder Piston Engine

Dynamic analysis of piston engines is considered one of the most important topics in mechanical engineering, as it plays a significant role in optimizing the performance and improving the efficiency of internal combustion engines. This analysis, by thoroughly examining the dynamic forces and torques acting on the moving components of the system including the piston, connecting rod, and crankshaft enables the prediction of system behavior under various operating conditions.

In this study, all influencing parameters have been considered, and the governing equations of the system have been derived and implemented as a computational code in MATLAB. This model is capable of accurately calculating and analyzing the distribution of various torques throughout the engine's working cycle. The mechanism of piston movements during one engine revolution, as well as the internal and external forces exerted during crankshaft rotation, are illustrated in The simulation, which accounts for phase differences between cylinders and incorporates real cylinder pressure data, allows for precise calculation of the instantaneous cylinder torque. To calculate the engine torque, the internal forces of the engine are first determined for a single-cylinder engine, and then extended to a six-cylinder engine. The resultant of the dynamic forces acting on the piston and the torsional vibrations is calculated with reference to [27]. In the mechanism of an internal combustion engine with a horizontally arranged cylinder layout, three main torques are identified: the gas pressure torque (M_{gas}), the inertia torque of different components (M_i), and the frictional torques (M_f). The resultant torque acting on the system can be expressed by Equation (1).

$$\Sigma M_{total} = M_{gas} + M_i - M_f \quad (1)$$

The frictional torque (M_f) arises from various sources of friction within the engine components and includes the friction of the camshaft system as well as the frictional torque generated by auxiliary attachments. the magnitude of frictional torques in different engines is less than 4% of the total torques produced by inertia and gas pressure, and thus, it can typically be neglected.

[DOI: 10.22068/ase.2026.721]

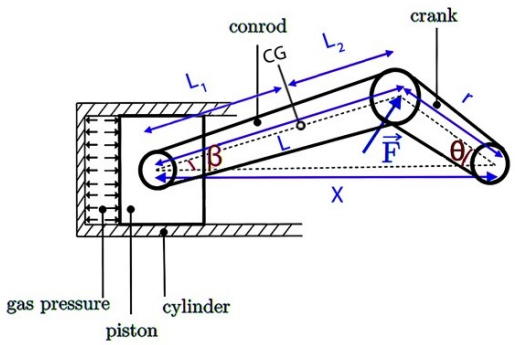

Figure 2: Dynamic model of the piston–crankshaft mechanism.

According to Figure 2, which illustrates the crankshaft–piston mechanism, θ, β, l and r represent the crank angle, the angle between the connecting rod and the piston, the connecting rod length, and the crank radius, respectively. In internal combustion engines, the torque generated at the crankshaft is influenced by three principal forces: gas pressure force, inertia force, and frictional force. These forces are transmitted and converted into rotational torque via the crankshaft–connecting rod–piston mechanism. Among these, the gas pressure force is directly produced by the combustion of fuel within the cylinder chamber. This force is calculated by multiplying the in-cylinder pressure by the cross-sectional area of the piston, as expressed in Equation (2).

$$F_{\text{gas}} = \frac{\pi D^2}{4} p_{\text{cyl}} \tag{2}$$

The in-cylinder pressure is a dynamic variable that changes with the piston position and the phase of the engine cycle. The stronger the combustion, the greater the gas pressure force will be. The inertia force corresponds to the accelerated motion of the system's moving components, including the piston, connecting rod, and a portion of the crankshaft. This force depends on the equivalent mass of these components and the linear acceleration of the piston. The piston acceleration itself is a function of the crankshaft's angular velocity and the geometry of the crankshaft–connecting rod mechanism. At high engine speeds, the effect of the inertia force increases significantly. The inertia force is generated by the piston mass (m_p) and the equivalent mass of the connecting rod (m_{eq-cr}), which is defined by Equation (3). In this equation, the equivalent mass of the connecting rod is introduced in Equation (4).

$$F_{\text{inertia}} = (m_p + m_{eq-cr})\ddot{x} \tag{3}$$

$$m_{eq-cr} = m_{cr} \times \left(\frac{L_2}{L_1 + L_2} \right) \tag{4}$$

Assuming a constant rotational speed of the crankshaft, the piston acceleration and the equivalent mass of the connecting rod are calculated according to Equation (5):

$$\ddot{x} = -r\omega^2 \left(\cos(\omega t) + \frac{r}{l}\cos(2\omega t) + \frac{r^3}{2l^3}\cos(4\omega t) \right) \tag{5}$$

According to the mechanism, the kinematic relationship between the crank angle and the connecting rod angle is given by Equation (6):

$$\beta = \sin^{-1}\left(\frac{1}{R}\sin(\omega t)\right) \tag{6}$$

In this equation, R represents the ratio of the connecting rod length to the crank radius ($R = l / r$), and ω denotes the angular velocity of the crankshaft in radians per second. According to Figure 2, by applying Newton's laws, the equilibrium equation for the crankshaft–connecting rod–piston mechanism in the horizontal direction can be formulated as Equation (7):

$$F_{\text{rod}} = \frac{1}{\cos(\beta)}\left(F_{\text{inertia}} + F_{\text{gas}}\right) \tag{7}$$

The torque applied to the crankshaft is the product of the tangential force exerted by the connecting rod and the crank radius (r):

$$\text{Torque} = r \times \left(\cos(\alpha) \times F_{\text{rod}}\right) \tag{8}$$

Equation (8) pertains to the total torque in a single-cylinder engine. To calculate the total torque in a multi-cylinder engine, the torque produced by each individual cylinder must be summed, taking into account the phase differences between their operating cycles. Since the nature of torque variations as a function of crank angle is identical for all cylinders (differing only in terms of phase shift) the torque characteristics of one cylinder are sufficient for determining the overall torque. By substituting the relevant relationships, simplifying, and generalizing the torque equation for a six-cylinder engine (where the total torque is obtained by summing the torques of each cylinder, each offset by a 120-degree phase difference), the expressions are given as Equation (9):

[DOI: 10.22068/ase.2026.721]

$$\text{Torque}_{\text{total}} = r\sum_{i=1}^{6}(A_i \times B_i) \tag{9}$$

Where:

$$A_i = \frac{\cos\left[90-(\omega t-\alpha_i)-\arcsin\left(\frac{\sin(\omega t-\alpha_i)}{R}\right)\right]}{\cos\left[\arcsin\left(\frac{a\sin(\omega t-\alpha_i)}{l}\right)\right]},$$
$$B_i = \frac{\pi D^2}{4}p_{\text{cyl}} - m\times r\times\omega^2\left[\cos(\omega t-\alpha_i)+\frac{1}{R}\cos 2(\omega t-\alpha_i)+\frac{1}{2R^3}\cos 4(\omega t-\alpha_i)\right] \tag{10}$$

α_i is the phase angle for each cylinder, which is defined by Equations (11).

$$(\alpha_i = \{0,\frac{2\pi}{3},\frac{4\pi}{3},2\pi,\frac{8\pi}{3},\frac{10\pi}{3}\}) \tag{11}$$

The specifications of the six-cylinder engine are presented in Table 1.

Table 1. Engine specifications

type	unit	6 cylinder inline
Piston diameter	mm	84
Crank shaft diameter	mm	81
Connecting rod	mm	135
Comperation ratio	-	9.7
Piston mass	gr	350
Connecting rod mass	gr	600
Rated power	hp (kW)	300 (224)
Rated torque	N·m	466
Operating speed range	rpm	2250–4500

In this study, the in-cylinder pressure of the engine was measured using a Kistler 6052C piezoelectric sensor and a 5064C amplifier. The sensor was mounted on the combustion chamber via a dedicated, sealed connector to provide the required resistance to high temperatures and pressures. Pressure data were recorded at a sampling rate of 2 MHz and synchronized with piston position data, which was obtained from an Autonics encoder with a resolution of 3600 pulses per revolution. The raw recorded data were processed using specialized software, and pressure versus crank angle diagrams were plotted. Figure 3 presents a sample pressure–crank angle diagram at an engine speed of 3000 rpm under ideal pressure conditions.

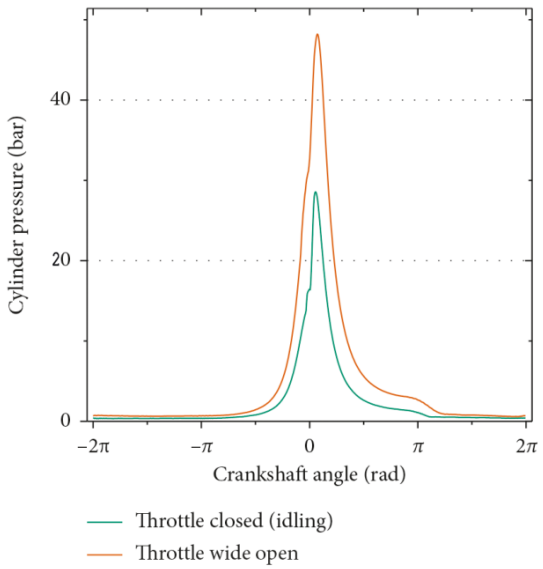

Figure 3: In-cylinder gas pressure diagram at an engine speed of 3000 rpm

By extracting the in-cylinder pressure at various engine speeds and applying Equations (8)–(11), the engine output torque is expressed as Equation (12):

$$M_e(t) = M_o + \Delta M \times \sin(\omega_e) \tag{12}$$

Where $M_e(t)$ is the engine torque, M_o is the mean torque produced as a function of engine performance, ΔM is the amplitude of torque fluctuation, and ω_e is the fundamental frequency corresponding to the engine crankshaft rotational speed.

Based on the engine specifications in Table 1, the mean and fluctuating torques at various engine speeds are listed in Table 2, and a sample output torque diagram is presented in Figure 4.

Table 2. Mean and fluctuating engine torque at various engine speeds

Fluctuating torque (N.m)	Mean torque (N.m)	Engine speed (rpm)
433	445	2250
445	466	3000
454.5	483.5	3750
463.5	491.5	4500

[DOI: 10.22068/ase.2026.721]

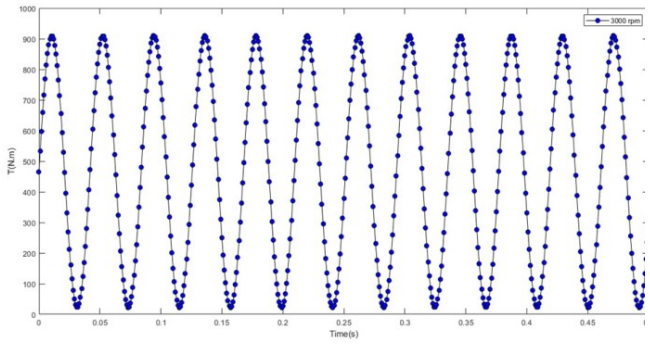

Figure 4: Torque versus crank angle diagram for the first cylinder at an engine speed of 3000 rpm

4. Governing Linear Equations for the Flywheel and Their Solution

As previously mentioned, the primary flywheel is mounted on the engine crankshaft, while the secondary flywheel is connected to the gearbox. The primary and secondary flywheels are modeled as inertial disks with moments of inertia j_1 and j_2, respectively. These two flywheels are coupled by torsional springs, which also exhibit damping effects. The input to this system is the engine torque, $M_e(t)$. The resisting torque acting on the system is the gearbox output torque, $M_g(t)$. The mathematical model of the dual-mass flywheel system is illustrated in Figure 5.

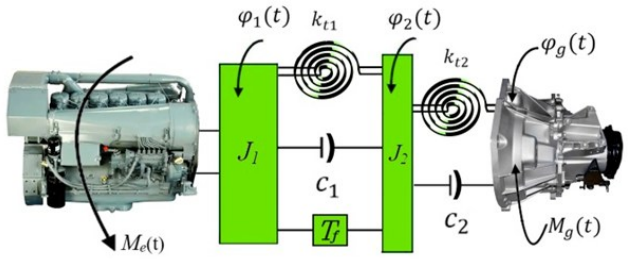

Figure 5: linear Free-body diagram model of the flywheel

As illustrated in Figure 5, the equations of motion for the dual-mass flywheel system can be modeled as a two-degree-of-freedom system using Newton's laws. The equations governing this system are presented as Equations (13) and (14).

$$J_1\ddot{\varphi}_1 + c_1(\dot{\varphi}_1 - \dot{\varphi}_2) + k_1(\varphi_1 - \varphi_2) - T_f = M_e(t) \quad (13)$$

$$J_2\ddot{\varphi}_2 + c_1(\dot{\varphi}_2 - \dot{\varphi}_1) + k_1(\varphi_2 - \varphi_1) + T_f + c_2(\dot{\varphi}_2 - \dot{\varphi}_g) + k_2(\varphi_2 - \varphi_g) = 0 \quad (14)$$

In these equations, φ_1 and φ_2 denote the absolute angular positions of the first and second flywheels, respectively. The derivatives of these variables, $\dot{\varphi}$ and $\ddot{\varphi}$, represent the angular velocity and angular acceleration of the flywheels, respectively. The coefficients k_1 and c_1, respectively, the stiffness and damping coefficients of the flywheel spring, while k_2 and c_2 are the stiffness and damping coefficients of the gearbox shaft. In the above equations, T_f is the frictional torque of the balls between the two flywheel discs, which prevents wear or collision between the discs. Assuming complete rolling of the ball along the circumference of rotation, as shown in Figure 6, the normal force acting on the ball's surface is the centrifugal force, defined by Equation (15):

$$F_f = m_b R_b \dot{\varphi}^2 \quad (15)$$

This force generates a frictional torque as described by Equation (16).

$$T_f = n\mu m_b R_b^2 \dot{\varphi}^2 \quad (16)$$

In Equation (16), n is the number of balls, μ is the coefficient of friction of the balls, m_b is the mass of each ball, R_b is the mean radius of the center of rotation of the balls, and $\dot{\varphi}$ is their angular velocity. In this model, it is possible to use steel bearing balls with a coefficient of friction ranging from 0.001 to 0.002. Alternatively, polymer balls such as POM, PP, and FKM can also be utilized. In addition to offering acceptable load-bearing capacity, these polymer balls exhibit a friction coefficient in the range of 0.05 to 0.2 [28].

In Equation (14), $c_2(\dot{\varphi}_g) + k_2(\varphi_g)$ represents the input torque to the gearbox, or $M_g(t)$. Equations (13) and (14) can be expressed in matrix form as Equations (17):

$$\begin{bmatrix} J_1 & 0 \\ 0 & J_2 \end{bmatrix}\begin{pmatrix} \ddot{\varphi}_1 \\ \ddot{\varphi}_2 \end{pmatrix} + \begin{bmatrix} c_1 & -c_1 \\ -c_1 & c_1 + c_2 \end{bmatrix}\begin{pmatrix} \dot{\varphi}_1 \\ \dot{\varphi}_2 \end{pmatrix} + \begin{bmatrix} k_1 & -k_1 \\ -k_1 & k_1 + k_2 \end{bmatrix}\begin{pmatrix} \varphi_1 \\ \varphi_2 \end{pmatrix} + \begin{bmatrix} -T_f \\ T_f \end{bmatrix} = \begin{pmatrix} M_e(t) \\ M_g(t) \end{pmatrix} \quad (17)$$

[DOI: 10.22068/ase.2026.721]

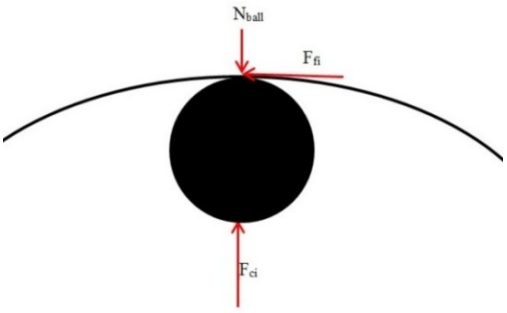

Figure 6: Centrifugal force acting on the ball

In these equations, it is assumed that the flywheel output is directly connected to the gearbox, and the engine output torque is considered as defined in Equation (12).

The inertia, stiffness, and damping parameters of the dual-mass flywheel used in the dynamic model are summarized in Table 3 These parameters define the nominal values employed in the linear and nonlinear simulations presented in this study.

Table 3. Design Parameters of the Dual-Mass Flywheel used in the dynamic model

Variable	value
J_1 (*kg.m²*)	0.055
J_2 (*kg.m²*)	0.006
K_1 (*Nm/rad*)	2800
K_2 (*Nm/rad*)	8500
C_1(*Nm.s/rad*)	0.3
C_2 (*Nm.s/rad*)	18

5. Spring Model in a Nonlinear System

As depicted in Figure 7, the spring can be considered as an independent subsystem. By employing the discretization method [5], the spring is divided into n elements (coils). Each element has a lumped mass and thus, the segmented spring system exhibits n degrees of freedom. These masses are interconnected by $n+1$ springs, all of which have the same stiffness coefficient k_i .

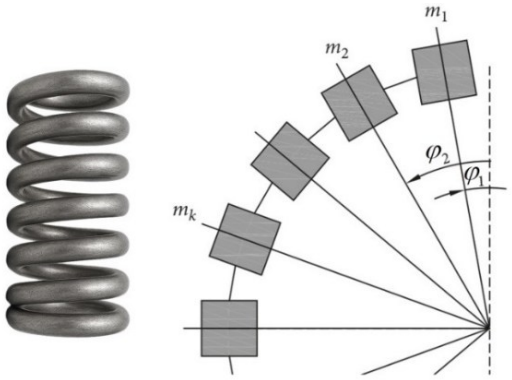

Figure 7: Discretized spring

In this discretized model, the entire sectoral spring structure is represented as a series of coils with lumped masses. The analysis of this model is based on the following three key assumptions [17]:

1. The behavior of each coil is modeled as linear.
2. The deformation of each coil is considered only along the circumferential direction of the circular sector.
3. The distribution of the frictional force between the spring and the flywheel wall is assumed to be uniform.

Figure 8 depicts the free-body diagram of a spring element, illustrating the forces acting upon it. In this figure, the elastic forces F_{Si+1} and $F_{S,i}$ correspond to the left and right adjacent coils, respectively. Additionally, the forces $F_{N,i}$, $F_{f,i}$, and $F_{c,i}$ represent the normal force, frictional force, and centrifugal force, respectively. The angle ϕ_i denotes the circumferential angle of the loaded coil. Parameters R and R_0 indicate the effective mean radius and the outer radius of the sectoral spring, respectively. The relationship between these radii and the spring diameter D_s is given by Equation 18:

$$R_0 = (R + \frac{D}{2}) \tag{18}$$

[DOI: 10.22068/ase.2026.721]

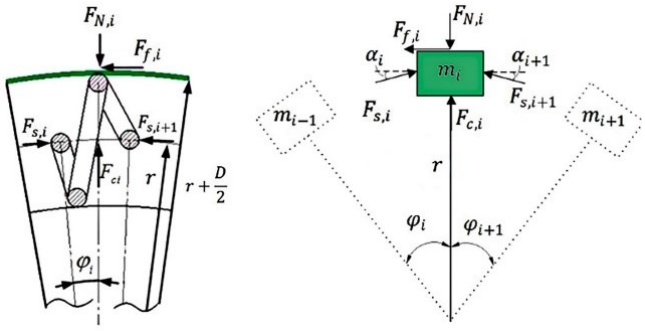

Figure 8: Free-body diagram of the i element of the discretized spring

By applying the equilibrium equations for forces in the horizontal direction (direction of rotation) and the vertical direction (perpendicular to the axis of rotation), Equations (19) and (20) are obtained for the *i* mass:

$$F_{S,i}\cos(\alpha_i)-F_{S,i+1}\cos(\alpha_{i+1}) \quad (19)$$
$$-F_{f,j}=m_i a_s=m_i r\ddot{\phi}_i$$

$$F_{C,i}-F_{N,i}+F_{S,i}\sin(\alpha_i)+F_{S,i+1}\sin(\alpha_{i+1})=0 \quad (20)$$

To calculate the normal force, Equation (20) is reformulated and presented as Equation (21):

$$F_{N,i}=F_{C,i}+F_{S,i}\sin(\alpha_i)+F_{S,i+1}\sin(\alpha_{i+1}) \quad (21)$$

In this relation, the angle α_i is calculated using Equation (22), in which $\varphi_{0,i}$ represents the angle between two consecutive mass elements of the spring in the unloaded state. Since the angular displacement of the spring may occur in either the rotational direction or the opposite direction, the absolute value is used when calculating the relative angle, while its sign (direction) is independently taken into account in the frictional torque equation $(i=1,\ldots,n+1)$.

$$\alpha_i=\frac{\phi_i}{2}=\frac{1}{2}(\varphi_{0,i}+\Delta\phi_i)=\frac{1}{2}(\varphi_{0,i}-|\phi_{i-1}-\phi_i|) \quad (22)$$

6. Nonlinear Model of the Dual-Mass Flywheel System

After the introduction of the linear model of the dual-mass flywheel where the first flywheel is assigned an inertia of J_{pri} and the second flywheel an inertia of $J_{\sec}$. this section focuses on the nonlinear modeling of the system. As previously stated, the torque produced by the engine is transmitted from the first flywheel to the second flywheel through the sector-shaped spring.

To achieve a more accurate representation of the nonlinear behavior of the spring within the dual-mass flywheel system, the sectorial spring is divided into *n* equal segments. Each of these segments is modeled as an individual coil and considered as an independent dynamic unit. Consequently, the entire system consists of n point masses m_i and $n+1$ springs, which are connected in series. Assuming viscous damping between the components, the damping and stiffness coefficients of each element are defined by Equations (23) and (24), respectively.

$$\frac{1}{K_{eq}}=\sum_{i=1}^{n}\frac{1}{K_i}\Rightarrow K_i=nK_{eq} \quad (23)$$

$$\frac{1}{C_{eq}}=\sum_{i=1}^{n}\frac{1}{C_i}\Rightarrow C_i=nC_{eq} \quad (24)$$

As previously mentioned, the frictional torque of the spring consists of two components: the elastic force and the centrifugal force. Since the centrifugal force depends on the angular velocity, the system includes terms of a nonlinear nature within the frictional torque. These nonlinear terms are subsequently added to the linear equations of the dual-mass flywheel model to yield a more accurate representation of its dynamic behavior.

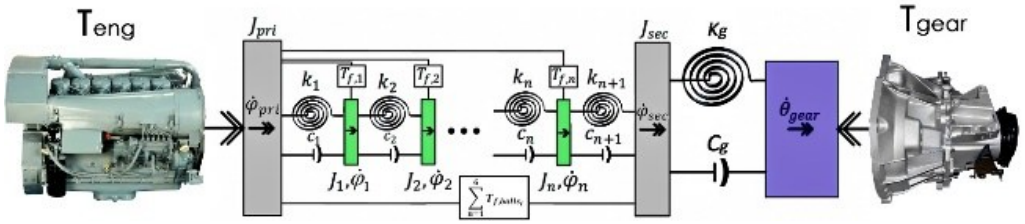

Figure 9: Free-body diagram of the dual-mass flywheel system with a spring of *n* degrees of freedom

The free-body diagram of this nonlinear system is shown in Figure 9. The number of degrees of freedom in this system is *n+2*. In this system, the absolute angular displacement of the primary flywheel is denoted by $\dot{\phi}_{pri}$, and for the secondary flywheel by $\dot{\phi}_{\sec}$. The frictional torque, $T_{\text{f,pri}}$, is equal to the sum of the frictional torques of all the mass elements of the spring. The angular

[DOI: 10.22068/ase.2026.721]

displacement, frictional torque, moment of inertia, stiffness, and viscous damping of each coil spring are represented, respectively, by the symbols $\dot{\phi}_i$, $T_{f,i}$, J_i, k_i and c_i.

According to Newton's second law, the equations of motion for this system are presented in Equations (25) to (27), where Equation (26) comprises n equations of motion. These equations are similar to those of the linear system, except that the frictional torque term has been added.

$$J_{\text{pri}}\ddot{\phi}_{pri} = T_{eng} - c_1(\dot{\phi}_{pri} - \dot{\phi}_1) - k_1(\phi_{pri} - \phi_1) - T_{f,pri} \tag{25}$$

$$J_{\text{pri}}\ddot{\phi}_{pri} = T_{eng} - T_{d,1} - T_{s,1} - T_{f,pri}$$

$$J_i\ddot{\phi}_i = T_{d,i} - T_{d,i+1} + T_{s,i} - T_{s,i+1} + T_{f,i} \quad , \quad i = 1,\cdots,n \tag{26}$$

$$J_{\text{sec}}\ddot{\phi}_{\text{sec}} = c_{n+1}(\dot{\phi}_n - \dot{\phi}_{\text{sec}}) - k_{n+1}(\phi_n - \phi_{\text{sec}}) - c_g(\dot{\phi}_{\text{sec}} - \dot{\phi}_g) - k_g(\phi_{\text{sec}} - \phi_g) \tag{27}$$

If the equations are rewritten in matrix form, the linear and nonlinear components can be represented as shown in Equation (28).

$$\underbrace{J\ddot{\varphi} + c.\dot{\varphi} + k.\varphi}_{linear} + \underbrace{C_N(\dot{\varphi})}_{nonlinear}.\dot{\varphi} = M \tag{28}$$

In these equations, the linear and nonlinear matrices are defined as given in Equations (29).

$$J.\ddot{\varphi} = \begin{bmatrix} J_{pri} & o & \cdots & o & o \\ o & J_1 & & o & o \\ \vdots & & \ddots & \vdots & \\ o & o & \cdots & J_n & o \\ o & o & & o & J_{sec} \end{bmatrix} \begin{bmatrix} \ddot{\varphi}_1 \\ \ddot{\varphi}_1 \\ \vdots \\ \ddot{\varphi}_n \\ \ddot{\varphi}_{sec} \end{bmatrix}$$

$$C.\dot{\varphi} = \begin{bmatrix} c_1 & -c_1 & \cdots & o & o \\ -c_1 & c_1 + c_2 & & o & o \\ \vdots & & \ddots & \vdots & \\ o & o & \cdots & c_n + c_{n+1} & -c_{n+1} \\ o & o & & -c_{n+1} & c_{n+1} + c_g \end{bmatrix} \times \begin{bmatrix} \dot{\varphi}_{pri} \\ \dot{\varphi}_1 \\ \vdots \\ \dot{\varphi}_n \\ \dot{\varphi}_{sec} \end{bmatrix}$$

$$k.\varphi = \begin{bmatrix} k_1 & -k_1 & \cdots & o & o \\ -k_1 & k_1 + k_2 & & o & o \\ \vdots & & \ddots & \vdots & \\ o & o & \cdots & k_n + k_{n+1} & -k_{n+1} \\ o & o & & -k_{n+1} & k_{n+1} + k_g \end{bmatrix} \begin{bmatrix} \varphi_{pri} \\ \varphi_1 \\ \vdots \\ \varphi_n \\ \varphi_{sec} \end{bmatrix}$$

$$C_N(\dot{\varphi}).\dot{\varphi} = \begin{bmatrix} c_{f.1} + \cdots + c_{f.n} & -c_{f.1} & \cdots & -c_{f.n} & o \\ -c_{f.1} & c_{f.1} & & o & o \\ \vdots & & \ddots & \vdots & \\ -c_{f.n} & o & \cdots & c_{f.n} & o \\ o & o & & o & o \end{bmatrix} \begin{bmatrix} \dot{\varphi}_{pri} \\ \dot{\varphi}_1 \\ \vdots \\ \dot{\varphi}_n \\ \dot{\varphi}_{sec} \end{bmatrix} = \begin{bmatrix} T_{f.1} + \cdots + T_{f.n} + T_{f.b} \\ -T_{f.1} \\ \vdots \\ -T_{f.n} \\ -T_{f.b} \end{bmatrix} \tag{29}$$

In the nonlinear component, the coefficient of frictional damping is defined as $C_{f,i} = \dfrac{\mu(r + \frac{D}{2})|F_{N,i}|}{|\dot{\theta}_{pri} - \dot{\theta}_i|}$, where μ is the friction coefficient, r and D are geometric parameters, and $F_{N,j}$ denotes the normal force applied to the spring.

7. Solution of the Equations Using the Newmark-Beta and Newton–Raphson Methods

The Newmark-beta method is a stable and widely used numerical technique for time integration in the dynamic analysis of structures and mechanical systems. This method estimates acceleration and angular velocity at the end of each time step through numerical approximations, making it suitable for solving time-dependent dynamic equations. The equation of motion for a system is expressed as shown in Equation (30):

$$T(t) = I\ddot{\theta}(t) + C\dot{\theta}(t) + K\theta(t) \tag{30}$$

In the Newmark method, the angular displacement and angular velocity at the time step $t + \Delta t$ are estimated using relations (31) and (32):

$$\dot{\theta}_{t+\Delta t} = \dot{\theta}_t + (1-\gamma)\Delta t \cdot \ddot{\theta}_t + \gamma\Delta t \cdot \ddot{\theta}_{t+\Delta t} \tag{31}$$

$$\theta_{t+\Delta t} = \theta_t + \Delta t \cdot \dot{\theta}_t + \beta\Delta t^2 \cdot \ddot{\theta}_{t+\Delta t} + \frac{(1-2\beta)}{2}\Delta t^2 \cdot \ddot{\theta}_t \tag{32}$$

The parameters β and γ control the numerical behavior and stability of the method. For unconditional stability, common values are given by relation (33):

$$\beta = \frac{1}{4}, \gamma = \frac{1}{2} \tag{33}$$

Using these values ensures the stability of the method for all time steps. To solve systems of nonlinear equations, the Newton method is

[DOI: 10.22068/ase.2026.721]

employed in the vector form given by relation (34):

$$\theta_{k+1} = \theta_k - J^{-1} f(\theta_k) \quad (34)$$

Here, J is the Jacobian matrix of the residual function, and $f(\theta_k)$ is the value of the residual at iteration k. This method is performed using numerical iterations until convergence is achieved, and when combined with time-stepping methods such as Newmark, it enables the solution of nonlinear dynamic equations.

8. Experimental Determination of Spring Damping Coefficient Using Modal Analysis

Modal analysis has become a key method for investigating the dynamic behavior of structures in engineering applications. This technique, which is based on measuring the frequency response function (FRF), determines modal parameters including natural frequencies, damping coefficients, and mode shapes by applying controlled excitation and recording the vibration response using sensors such as accelerometers. In this study, experimental modal analysis was used to calculate the damping coefficient (C_1) of the spring.

Modal testing requires specialized equipment, including an excitation device (impact hammer), measurement sensors (accelerometers), and a vibration analyzer. In this research, a YE6268-36 vibration analyzer was used, which enables high-precision processing of vibration signals. The device used provides 36 input channels for connecting accelerometers and utilizes FFT analysis capability for signal processing. The sensor output data are received in analog form and, after amplification and conversion to digital data, are processed by N-modal software under Windows. This software allows for the display of frequency spectra and the calculation of modal parameters.

To determine the damping coefficient of the spring, modal testing was performed in accordance with established standards. As shown in Figure 10, the spring was suspended freely in air (free-free condition) using strings to minimize the effects of external damping. The structure was excited using an impact hammer, and the dynamic response was measured by an accelerometer attached to the spring. In this experiment, after three repeated tests and data analysis using N-modal software, the average damping coefficient of the spring was found to be 0.05, which is consistent with theoretical values. Figure11 shows the measured response of the spring to hammer excitation. The results of this experiment were used as input data for the dynamic modeling of the dual-mass flywheel.

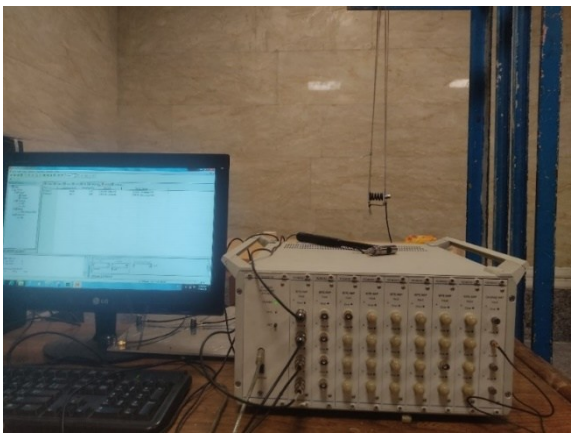

Figure 10: Structural Configuration during Modal Testing

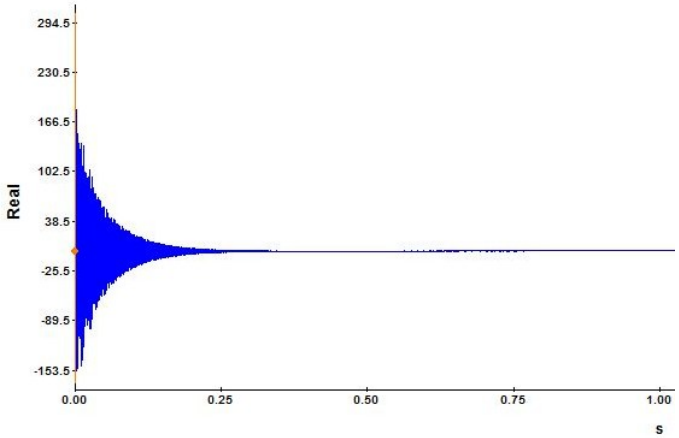

Figure 11: Time-domain response of the spring to impact hammer excitation

9. Analysis and Evaluation of Nonlinear Modeling Effects

For accurate dynamic modeling of the dual-mass flywheel system, a segmental spring has been employed as the principal element for torque transmission and vibration absorption between the two masses. For the modeling and simulations, the following parameter values were employed: primary flywheel inertia j_1=0.05 ($kg.m^2$), secondary flywheel inertia j_2=0.007 ($kg.m^2$), flywheel spring stiffness k_1=6360 (Nm/rad), gearbox shaft stiffness k_2=9650 (Nm/rad), flywheel spring damping coefficient c_1=0.05 ($Nm.s/rad$) (experimentally determined in Section 8), and gearbox shaft damping coefficient c_2=12

[DOI: 10.22068/ase.2026.721]

(*Nm.s/rad*).To achieve a realistic simulation in the nonlinear model, it is necessary to fully define the physical and geometric properties of this spring. Table presents the numerical values of the mechanical and geometric parameters of the segmental spring used in the analysis. These values have been utilized as input to the dynamic model and play a decisive role in determining the system response under various operating conditions.

The diagrams presented in Figure 12 and Figure 13 compare the results of linear and nonlinear analyses of the transmitted torque in the dual-mass flywheel system under two different angular velocities 2250 and 3000 rpm. The purpose of this comparison is to evaluate the accuracy and differences in the dynamic behavior of the system when employing nonlinear modeling as opposed to linear simplifications.

Table 4. Physical and Geometric Parameters of the Segmental Spring

m [kg]	μ [−]	r [m]	D [m]
0.03	0.1	0.08	0.02

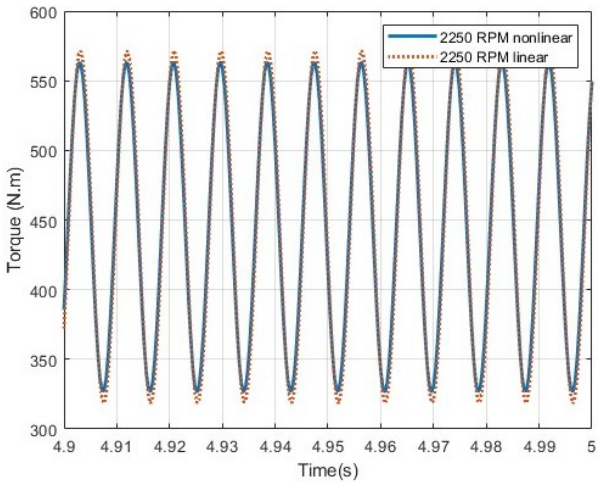

Figure 12: Comparison of linear and nonlinear analysis of transmitted torque at an angular velocity of 2250 rpm

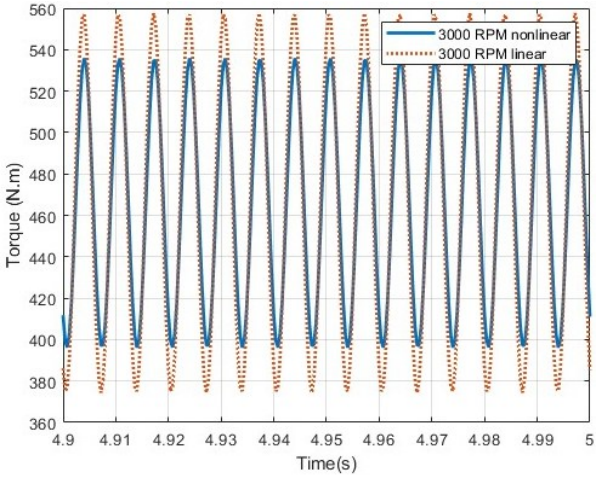

Figure 13: Comparison of linear and nonlinear analysis of transmitted torque at an angular velocity of 3000 rpm

In this diagram, the transmitted torque between the two flywheels is shown over a short time interval from 4.9 to 5 seconds. In this case, the nonlinear model (depicted by the solid blue line) and the linear model (shown as the orange dashed line) exhibit very similar behaviors. The amplitude and frequency of oscillations are nearly identical for both models, indicating that at this speed, the nonlinear effects (stemming from the nonlinear damping of the segmental spring) have not yet become prominent. Nevertheless, close examination reveals that the nonlinear model provides a smoother and more realistic response, with slightly lower peak torque values compared to the linear model. Although this difference appears minor, it can lead to improved predictions of component lifespan and vibrational response in precise and sensitive applications.

With increasing rotational speed to 3000 rpm, the difference between the two models becomes noticeably more significant. As observed in the diagram, the linear model exhibits a larger oscillation amplitude and demonstrates a more oscillatory behavior, whereas the nonlinear model yields a more controlled response. This phenomenon is primarily due to the more pronounced influence of nonlinear factors such as internal friction and the speed-dependent nonlinear damping of the segmental spring, which are neglected in the linear model. In other words, at this higher speed, the linear model exaggerates the predicted torque oscillations and fails to accurately represent the actual system behavior.

[DOI: 10.22068/ase.2026.721]

10. Analytical Comparison of Single-Mass and Dual-Mass Flywheels with Identical Inertia

In this section, in order to investigate the effect of flywheel structure on the dynamic response of the power transmission system, two types of flywheels, a conventional single-mass flywheel and a dual-mass flywheel are compared. A key point in this analysis is that both types of flywheels are considered to have identical moment of inertia, so that the specific effect of the internal structure can be analyzed independently. Figure 14 presents a schematic of the single-mass flywheel.

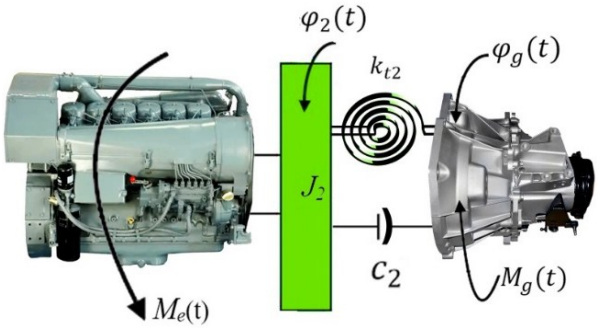

Figure 14: Schematic of a conventional single mass flywheel

Based on the torque response diagrams (Figure 15 for the conventional single-mass flywheel and Figure 16 for the dual-mass flywheel) and as summarized in Table 5, the following observations can be made:

Table 5. Quantitative comparison of the conventional and dual-mass flywheels

Rotational speed (rpm)	Type of flywheel	Minimum torque (N·m)	Maximum torque (N·m)	Torque oscillation amplitude (N·m)
2250	Conventional	225	665	440
	Dual-mass	325	560	235
3000	Conventional	345	585	240
	Dual-mass	395	535	140
3750	Conventional	405	560	155
	Dual-mass	435	530	95

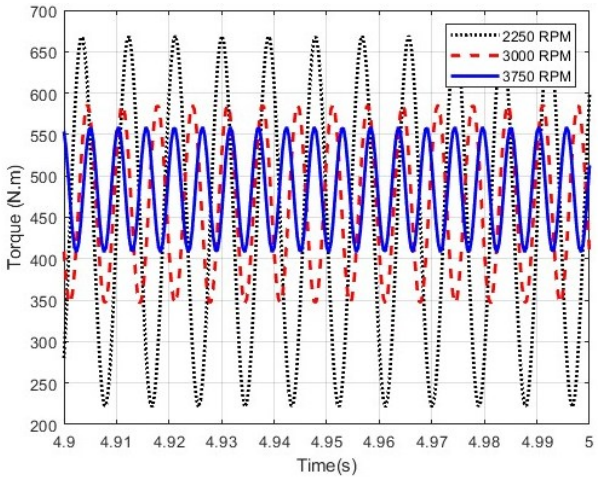

Figure 15: Amplitude of steady-state torque oscillations in the conventional flywheel

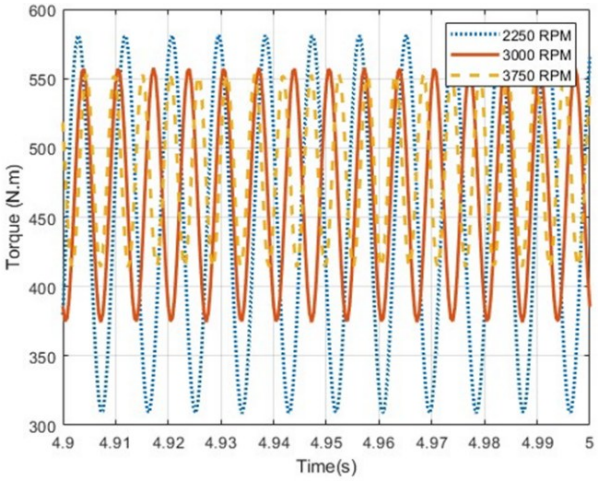

Figure 16: Amplitude of steady-state torque oscillations in the dual-mass flywheel

- The amplitude of torque oscillations in the single-mass flywheel is significantly greater than that of the dual-mass flywheel.
- This difference is present across all examined rotational speeds, including 2250, 3000, and 3750 rpm.
- The system equipped with a dual-mass flywheel exhibits a smoother response, with its torque fluctuations effectively damped.

These results clearly demonstrate that the internal mechanical structure of the dual-mass flywheel particularly the spring and damping system between the two masses plays a crucial role in absorbing and reducing engine torsional vibrations, without the need to increase the overall system inertia.

In continuation of this study, and in order to evaluate the effect of mass moment of inertia on the performance of the single-mass flywheel, the moment of inertia of this flywheel was increased

[DOI: 10.22068/ase.2026.721]

to the extent that the amplitude of its output torque oscillations became equal to that of the dual-mass flywheel. As a result, the moment of inertia of the single-mass flywheel was raised to 0.095. Although this increase in inertia led to a partial convergence of the dynamic behavior of the single-mass flywheel with that of the dual-mass flywheel, achieving this inertia value required increasing the mass of the single-mass flywheel to approximately 8.5 kg, which is nearly 1.8 times greater than that of the dual-mass flywheel.

These findings indicate that, when using a single-mass flywheel, reducing torque oscillations necessitates a significant increase in the system mass. In contrast, the dual-mass flywheel is capable of more effectively damping oscillations with a lower mass, thanks to its internal structure. This underscores the engineering advantages of the dual-mass flywheel design, as it delivers superior dynamic performance without adding extra weight.

According to the results presented in Table 5, the dual-mass flywheel exhibits more efficient performance in reducing the amplitude of torque oscillations compared to the single-mass type under equal moment of inertia conditions. Specifically, at rotational speeds of 2250, 3000, and 3750 rpm, the torque oscillation amplitude in the dual-mass flywheel is respectively 46%, 41%, and 38% lower than that of the single-mass counterpart. These findings highlight the superior capability of the dual-mass flywheel in enhancing the dynamic performance of power transmission systems.

11. Experimental Testing on the Dynamometer Stand

To evaluate the performance of the designed dual-mass flywheel, comprehensive experimental tests were conducted on a dynamometer stand equipped with speed and torque control capabilities. The experimental setup consisted of a closed-loop controlled eddy current electric dynamometer with an accuracy of ±0.5%. In this study, two operating speeds 2250 and 3000 rpm were selected as the engine's operational range. The tests were conducted up to 3000 rpm due to limitations of the torque sensor. These sensors typically use strain gauges installed on a flexible shaft to measure the deformation induced by torque and convert it into electrical signals.

The test protocol was as follows: the system was first started at a baseline speed of 2000 rpm without load, and after reaching thermal steady-state conditions, the speed was increased to the desired value. The load was then gradually applied over 30 seconds to the specified level, and data was recorded for 60 seconds under steady-state conditions. To ensure repeatability, each test was performed three times. The measured parameters included output torque, engine temperature, engine speed, temperature at critical engine points, and others. The torque meters equipped with strain-gauge transducers provided a measurement accuracy of ±0.1%. The schematic of the test chamber and dynamometer is shown in Figure 17.

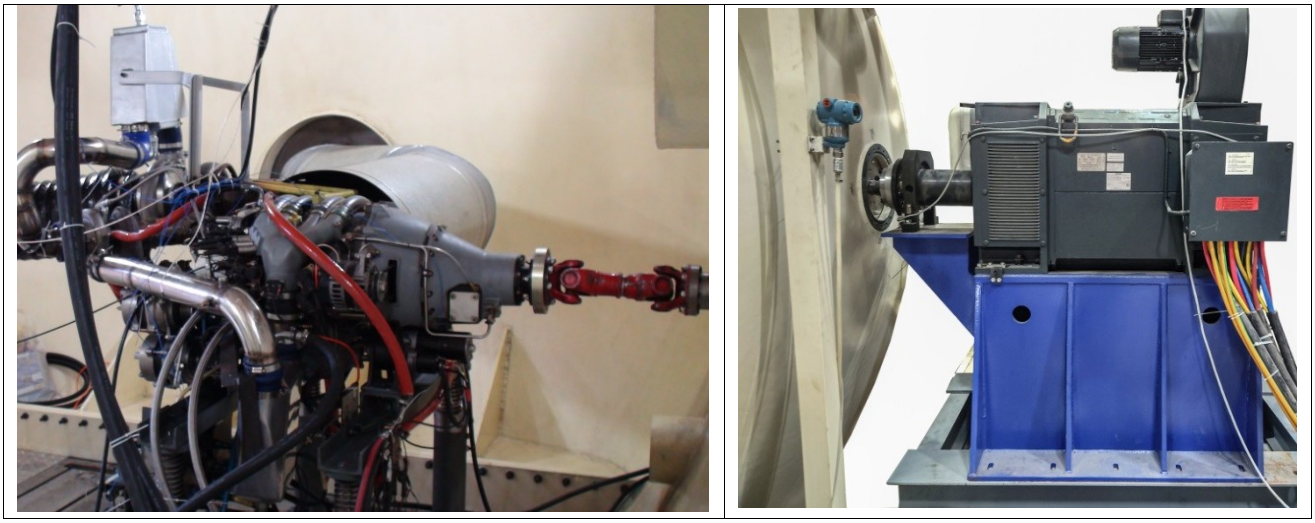

Figure 17: Overview of the dynamometer and test chamber

Figure 18 illustrates the variations in the input and output torque of the flywheel under constant dynamometer loading on the engine, examined at two speeds: 2250 and 3000 rpm. The experimental data presented in Table 6 provide precise quantitative information from the conducted tests, with a representative sample shown in Figure 18. Analysis of the data indicates

[DOI: 10.22068/ase.2026.721]

that the dual-mass flywheel system demonstrated optimal performance under all experimental conditions.

The system achieved its highest level of damping at the higher speed. Specifically, at 2250 rpm, despite the engine torque oscillation amplitude being 433 N·m, the system managed to reduce the output oscillation amplitude to 101.2 N·m, corresponding to a damping efficiency of 76.6%. This performance significantly improved at higher speeds; at 3000 rpm, the damping increased to 89.9%, corresponding to a decrease in oscillation amplitude from 445 N·m to 45 N·m at the flywheel output.

Table 6. Experimental dynamometer test data

Engine speed (rpm)	Engine torque oscillation amplitude (N.m)	Experimental output torque oscillation amplitude of the flywheel (N.m)	Experimental damping ratio (%)
2250	433	101.20	76.62
3000	445	45	89.90

To further assess the accuracy of the analytical models, the experimental results were compared with both linear and nonlinear simulations. This comparison is presented in Table 7, which shows that the nonlinear model provides a closer agreement with experimental data across the tested operating speeds.

Table 7. Comparison of flywheel output torque oscillation amplitude damping (%) by analytical and experimental methods

Engine speed (rpm)	2250	3000
Experimental (%)	76.62	89.90
Linear method (%)	71.28	79.47
Nonlinear method (%)	72.40	83.92
Linear error (%)	6.9	11.6
Nonlinear error (%)	5.5	6.6

The results of these experiments clearly demonstrate that the designed dual-mass flywheel exhibits excellent performance across all operational ranges. Under constant power conditions, the system not only maintains its stability, but also shows continuous improvement in damping performance as rotational speed increases. These characteristics make the system an ideal choice for industrial applications that require stable operation over a wide range of operating conditions.

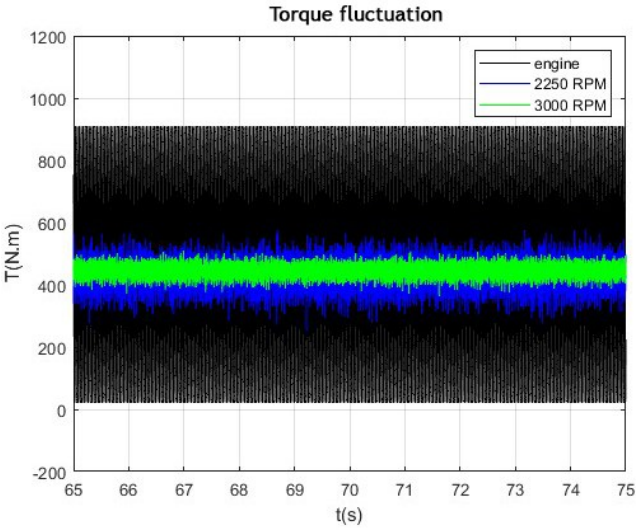

Figure 18: Engine and flywheel torque during loading

12. Conclusion

In this study, the performance of a novel dual-mass flywheel for reducing torque oscillations in piston engine power transmission systems was investigated using analytical, numerical, and experimental approaches. The results demonstrate that the proposed dual-mass flywheel effectively attenuates torsional vibrations while maintaining a lower overall system mass compared to a conventional single-mass flywheel.

Experimental results indicated that the dual-mass flywheel reduced the torque oscillation amplitude by 46% at 2250 rpm, 41% at 3000 rpm, and approximately 38% at 3750 rpm relative to the single-mass configuration. Achieving comparable damping performance with a single-mass flywheel would require up to an 80% increase in mass, which highlights the superior efficiency of the proposed design.

Furthermore, a comparison between experimental data and analytical predictions showed that the nonlinear model provides closer agreement with experimental results than the linear model. At engine speeds of 2250 rpm and 3000 rpm, the experimentally measured damping ratios of the flywheel output torque oscillations were 76.62% and 89.90%, respectively. In comparison, the linear model predicted damping ratios of 71.28% and 79.47%, while the nonlinear model predicted 72.40% and 83.92% at the same speeds. The corresponding prediction errors of the nonlinear model (5.5% and 6.6%) were lower than those of the linear model (6.9% and 11.6%), confirming the higher accuracy of the nonlinear formulation.

Overall, the results confirm that the proposed dual-mass flywheel offers an effective and

[DOI: 10.22068/ase.2026.721]

lightweight solution for controlling torsional oscillations in piston engines, and that nonlinear modeling provides a more reliable tool for predicting the dynamic behavior of such systems.

List of symbols

Symbol	Description
C_1	Viscous damping coefficient of the dual-mass flywheel spring (Nm·s/rad)
C_2	Viscous damping coefficient of the gearbox shaft (Nm·s/rad)
D	Diameter of spring (m)
F_N	Normal force acting on the ball (N)
F_c	centrifugal force acting on the ball (N)
F_s	elastic force acting on the ball (N)
J_1	Moment of inertia of the primary flywheel (kg·m²)
J_2	Moment of inertia of the secondary flywheel (kg·m²)
K_1	Torsional stiffness of the dual-mass flywheel spring (Nm/rad)
K_2	Torsional stiffness of the gearbox shaft (Nm/rad)
m	Mass of each spring (kg)
m_{cr}	mass of the connecting rod
M_e	Engine output torque (Nm)
m_i	Lumped mass of the i-th spring element (kg)
m_p	mass of the piston
n	Number of balls or number of discretized spring elements
r	Mean radius of ball rotation (m)
T_f	Frictional torque generated by the balls (Nm)
i	Index of discretized spring element
θ_1	Angular displacement of the primary flywheel (rad)
θ_2	Angular displacement of the secondary flywheel (rad)
μ	Coefficient of friction of the spring
ω_1	Angular velocity of the primary flywheel (rad/s)
ω_2	Angular velocity of the secondary flywheel (rad/s)

13. References

[1] L. Chen WS, Z.y. Chen. Modeling and Experimental Study on Dynamic Characteristics of Dual-Mass Flywheel Torsional Damper. Shock and Vibration. 2019:13.

[2] C.L. Gaillard RS. Dynamic analysis of automotive clutch dampers. Applied Acoustics. 2000;60(4)

[3] N. Cavina GS. Analysis of a Dual Mass Flywheel System for Engine Control Applications. SAE International. 2004;113(7):280-6.

[4] Schweinfurt HB. Systematic search for and vibratory assessment of new action principles for alternative rotary vibration decoupling systems in the passenger car driveline. Drive System Technique. 2004;6:3-12.

[5] T. Kim HS, S. Hwang, H. Kim. Analysis of Dual Mass Flywheel using Discrete Arcspring Model. Engineering Materials. 2006;326-328: 1607-10.

[6] L Zeng, J Liu, Z Wan, L Song, X Yuan. Modeling and vibration characteristics analysis of a DMF rotor system. J Mech Sci Technol. 2022;36(6):2799-2810.

[7] H. Jianjun QD, Z. Yusheng, L. Yonggang. Study on natural torsional vibration characteristics of dual mass-flywheel radial spring type torsional vibration damper. SAE Technical Paper; 2009. Report No.: 0148-7191.

[8] U. Schaper OS, T. MaIll, V. Blessing. Modeling and torque estimation of an automotive Dual Mass Flywheel. american control conference; USA2009.

[9] T.S. Kang SKK, K.P. Ha. Development of the displacement measuring system for a dual mass flywheel in a vehicle. Automobile Engineering 2009;223:1273-4.

[10] D. CHEN ZH, C. Ling, W. Sun Torsion stiffness calculation and optimization design of arc helix spring of dmf. China Mechanical Engineering. 2010;21(14):1676.

[11] Mahl T, Sawodny O. Modelling of an automotive dual mass flywheel. IFAC Proceedings Volumes. 2010 Jan 1;43(18):517-23.

[12] S. Mohire RB. Evaluation of interdependent behavior of dual mass flywheel (DMF) and engine

[DOI: 10.22068/ase.2026.721]

starting system. SAE Technical Paper; 2010. Report No.: 0148-7191.

[13] Lee Y-J, Shim T-Y, Lee K-O, Hur M-D, Kang S-S. Effect of induction heating on fatigue life of drive plate for dual mass flywheel. Journal of Mechanical Science and Technology. 2013;27(8):2323-9.

[14] Chen Z, Chen Z, Mao Y, Shi W, Zhang G. Control research of power train torsional vibration based on magneto-rheological fluid dual mass flywheel. SAE Technical Paper; 2014.

[15] S. Shojaei, M. Hoseinalipur, H. Chamani. Torsional Vibrations Analysis of the Set of Linear Six Cylinder Diesel Engine Crankshaft and Validation of Its Results. 2014;10(3)

[16] LQ Song, LP Zeng, SP Zhang, JD Zhou, HE Niu. Design and analysis of a dual mass flywheel with continuously variable stiffness based on compensation principle. Mechanism and machine theory. 2014 Sep 1;79:124-40.

[17] L Chen, R Zeng, Z Jiang. Nonlinear dynamical model of an automotive dual mass flywheel. Advances in Mechanical Engineering. 2015 , 9;7(6).

[18] Y. Wang Xp, S. Huang , S. Deng. Design and analysis of a multi-stage torsional stiffness dual mass flywheel based on vibration control. Applied Acoustics. 2016;104:172–81.

[19] X. Tang XH, W. Yang, H. Yu. Novel torsional vibration modeling and assessment of a power-split hybrid electric vehicle equipped with a dual-mass flywheel. IEEE transactions on vehicular technology. 2017;67(3).

[20] L. He CX, S. Chen, J. Guo, Y. Liu. Parametric Investigation of Dual-Mass Flywheel Based on Driveline Start-Up Torsional Vibration Control. Shock and Vibration. 2019;2019:1-12.

[21] G. M. Gharehbolagh ARB, P. Safarpour, Y. Abbaszadeh. Nonlinear analysis of torsional vibrations of dual mass flywheel in a three-cylinder engine. Proceedings of the Institution of Mechanical Engineers, Part K: Journal of Multi-body Dynamics. 2023;237(1):3-15.

[22] B. Kindratskyy RL, O. Osmak. Influence of vehicle acceleration intensity on dual-mass flywheel elements and transmission load. Transport Technol. 2022;3(1):65-76.

[23] S. Vlase MM, A. Elkhalfi, P. Ailawalia. Mathematical model for dynamic analysis of internal combustion engines. Journal of Computational Applied Mechanics. 2023;54(4):607-22.

[24] Berbyuk V. Design optimization of torsional vibration absorbers for heavy-duty truck drivetrain systems. Vibration. 2019 Jul 12;2(3):240-64.

[25] Berbyuk V. Weight-vibration pareto optimization of a triple mass flywheel for Heavy-Duty truck powertrains. Machines. 2020 Aug 31;8(3):50.

[26] Berbyuk V. Weight-Vibration Pareto Optimization of a Dual Mass Flywheel. Journal of Mathematical Sciences. 2022 May;263(1):1-4.

[27] Heywood J. Internal Combustion Engine Fundamentals. 2 ed: McGraw-Hill Education; 2018.

[28] D. Miler MH, Z. Domitran, D. Žeželj. Prediction of friction coefficient in dry-lubricated polyoxymethylene spur gear pairs. Mechanism and Machine Theory 2019;138:205–22.

[DOI: 10.22068/ase.2026.721]